

Constraints on Tidal Quality Factor in Kepler Eclipsing Binaries using Tidal Synchronization: A Frequency-Dependent Approach

Ruskin Patel,^{1*} Kaloyan Penev,^{1†} Joshua Schussler¹

¹*Department of Physics, University of Texas at Dallas, Richardson, Texas*

Accepted XXX. Received YYY; in original form ZZZ

ABSTRACT

Tidal dissipation in binary systems is the primary source for synchronization and circularization of the objects in the system. The efficiency of the dissipation of tidal energy inside stars or planets results in significant changes in observed properties of the binary system and is often studied empirically using a parameter, commonly known as the modified tidal quality factor (Q'_\star). Though often assumed constant, in general that parameter will depend on the particular tidal wave experiencing the dissipation and the properties of the tidally distorted object. In this work we study the frequency dependence of Q'_\star for Sun-like stars. We parameterize Q'_\star as a saturating power-law in tidal frequency and obtain constraints using the stellar rotation period of 70 eclipsing binaries observed by Kepler. We use Bayesian analysis to account for the uncertainties in the observational data required for tidal evolution. Our analysis shows that Q'_\star is well constrained for tidal periods > 15 days, with a value of $Q'_\star \sim 10^8$ for periods > 30 days and a slight suggested decrease at shorter periods. For tidal periods < 15 days, Q'_\star is no longer tightly constrained, allowing for a broad range of possible values that overlaps with the constraints obtained using tidal circularization in binaries, which point to much more efficient dissipation: $Q'_\star \sim 10^6$.

Key words: (stars:) binaries: eclipsing–stars: solar-type–stars: rotation–stars: kinematics and dynamics–stars: interiors

1 INTRODUCTION

The study of tides is imperative in understanding the observed properties of binary systems, as the evolution of the spins and orbital parameters in binaries are often strongly influenced by tides. The discovery of hot-Jupiter exoplanets (Mayor & Queloz 1995; Marcy & Butler 1996) has rekindled interest in understanding the efficiency of tidal dissipation as tides can provide a reasonable explanation for their observed short periods and close-to-circular orbits (Rasio & Ford 1996; Fabrycky & Tremaine 2007; Beaugé & Nesvorný 2012; Vick et al. 2019).

Under the influence of tides, orbits can either shrink or expand depending on the spins of the binary members and on the orbit. In circular orbits for example, if a given component of the binary spins slower than the orbit, tides will transfer angular momentum from the orbit to the spin of the object, leading to orbital decay. If an object is spinning faster than the orbit, tides cause it to spin down towards synchronous rotation. Reliable estimation of the efficiency of tidal dissipation in such systems is important for understanding either the survival of hot Jupiters (Debes & Jackson 2010; Hamer & Schlaufman 2019) or the halting of the inward migration (Lin et al. 1996; Alvarado-Montes 2022), or both. If the secondary object is a star, tides usually do not threaten the long-term survival of the system, because typically binary star systems have enough angular momentum to achieve a state of minimum energy; this may manifest itself in three major observational properties of the binary system:

- (i) **Tidal Synchronization** → The rotation period of both stars is equal to the orbital period.
- (ii) **Tidal Circularization** → Eccentricity of the orbit is close to zero.
- (iii) **Tidal Inclination** → The angular momentum vector of the stars align with the angular momentum vector of orbit.

There are many suggested tidal dissipation processes. They can generally be divided into two classes depending on the physical mechanism responsible for the dissipation: equilibrium tides (Zahn 1989; Goldreich & Keeley 1977; Penev et al. 2009; Ogilvie & Lesur 2012; Duguid et al. 2020; Vidal & Barker 2020), where the energy dissipation is primarily through turbulent viscosity, and dynamical tides (Zahn 1975; Goodman & Dickson 1998; Rieutord & Valdettaro 2010; Ogilvie 2013; Essick & Weinberg 2016; Fuller et al. 2016; Barker 2020; Ma & Fuller 2021), where the waves excited inside the star interact with tidal perturbations and dissipation is either through turbulent viscosity or wave breaking. Empirically, the efficiency of dissipation is often parameterized by what is commonly known as the *tidal quality factor*: Q . The inverse of Q is the ratio of the energy dissipated from a tidal bulge in a single orbit to the tidal energy stored in the tidal bulge (Goldreich & Soter 1966). Lower values of Q correspond to high dissipation and vice versa. In practice, parametric studies of tides use a modified tidal quality factor: $Q' = Q/k_2$ (Ogilvie 2012), where k_2 is the second order love number. In this paper, we use Q'_\star to refer to the modified tidal quality factor of a given star.

The equilibrium theory of tides assumes that the star maintains hydrostatic equilibrium while perturbed by the tidal forces. The

* E-mail: ruskin.patel@utdallas.edu

† E-mail: kaloyan.penev@utdallas.edu

quadrupole tidal field of the companion deforms the primary, leading to the formation of tidal bulges. Under the assumption of weak tides, one can further decompose the time dependence of the tidal potential as a Fourier series, thinking of each term in the series as driving an independent tidal bulge and contributing to the dissipation as a simple superposition. Earlier studies assumed that the perturbations in the star respond to the tidal potential with a constant lag in either phase or time (Zahn 1975; Hut 1981; Alexander 1973; Eggleton et al. 1998). In general however, each tidal wave can experience different dissipation depending on its tidal frequency:

$$\Omega_{\text{tide}} = m\Omega_{\text{orbit}} - n\Omega_{\star} \quad (1)$$

where m and n are integers, Ω_{orbit} is the orbital frequency and Ω_{\star} is the spin frequency of the star. As a result, the lag, which is inversely related to Q'_{\star} , is a frequency-dependent parameter rather than a constant, with the exact frequency dependence determined by the dissipation mechanism.

Even though dynamical tide models do not strictly follow the above picture, the resulting energy and angular momentum exchange can still be modeled by an effective Q'_{\star} with an associated frequency dependence (see Ogilvie 2012 for more thorough discussion).

In this study we focus on stars with radiative cores and convective envelopes. (Goodman & Dickson 1998, Lecoanet & Quataert 2013, and others) argue that in such stars, tides can excite g-modes at the boundary of the two zones, which travel inward through the core. If the wave amplitude is high enough they can break, dissipating energy and depositing angular momentum. The resulting effective tidal quality factor has a frequency dependence given by $Q'_{\star} \propto \Omega_{\text{tide}}^{-2.6}$ (Barker & Ogilvie 2011). If the wave amplitude is not high enough for wave breaking to take place, Essick & Weinberg (2016) showed that dissipation can still occur through the excitation of a network of daughter, grand-daughter, etc. modes and $Q'_{\star} \propto \Omega_{\text{tide}}^{-2.4}$.

Ogilvie & Lin (2004); Ogilvie & Lin (2007); Ogilvie (2009); Rieutord & Valdettaro (2010); Barker (2020) proposed a different dissipation mechanism, driven by damping of tidally excited inertial waves by turbulent viscosity in the convective zone of stars resulting in enhanced dissipation compared to equilibrium tides. Since inertial waves only exist with frequencies $|\omega| < |2\Omega|$, where Ω is the spin frequency of the star, the dissipation will only be enhanced for tidal frequencies in this range. The resulting dissipation is predicted to be highly frequency dependent with a dense spectrum of peaks. A widely used method for accounting for enhanced dissipation due to inertial waves is averaging over the dissipation spectrum in the frequency domain to calculate the net contribution of Q'_{\star} from dynamical tides (Ogilvie 2013).

Yet another dissipation mechanism invokes resonance locking if the tidal frequency is in resonance with a low-frequency inertial wave in the convective envelope or a standing g-mode in the radiative zone (Witte & Savonije 1999, 2001; Fuller et al. 2016; Fuller 2017). This could lead to enhanced dissipation if the resonance is held for a long period without breaking the lock. Most recently, Ma & Fuller (2021) predict resonance locking can be modeled with $Q'_{\star} \propto \Omega_{\text{tide}}^{13/3}$.

Validating and clarifying this broad range of models requires measuring Q'_{\star} from observations. This is far from the first effort to accomplish this. Recently, Bolmont et al. (2017) presented a tidal evolution model restricted to circular orbits, with zero spin-orbit misalignment. The authors use the frequency-averaged dissipation due to inertial waves (Ogilvie 2012) with a constant time lag model (Hut 1981; Eggleton et al. 1998) to approximate Q'_{\star} as a constant parameter. Benbakoura et al. (2019) makes a distinction between the outer convective and inner radiative zones of the stars to allow for angular momentum exchange between the two zones. The authors

also improve on the Bolmont et al. (2017) model by differentiating between Q'_{\star} obtained from equilibrium tides and dynamical tides, but the tidal potential is restricted to only lower-order eccentricity terms with no spin-orbit misalignment.

In this paper we explore the dependence of Q'_{\star} on tidal frequency using low-mass eclipsing binaries observed by Kepler, with parameters taken from Windemuth et al. (2019), combined with rotation period measurements of the primary star by Lurie et al. (2017). Unlike the earlier efforts mentioned above, we do not assume a particular tidal model, but instead assume a generic parameterization of frequency dependent Q'_{\star} . We use Bayesian analysis to fully account for observational uncertainties, and a tidal evolution model designed to analyze any parametric dependence of Q'_{\star} on binary properties, along with the effects of higher order eccentric terms in tidal potential, changes in internal structure of the star, and spin-down of the star due to magnetic winds.

The rest of the paper is as follows. In Section 2, we provide details of the tidal evolution model used for the analysis. Section 3 describes the source of the observational data used. Section 4 shows the formalism for the frequency-dependent Q'_{\star} model. Section 5 describes the methodology for Bayesian analysis. Our results are presented in Section 6. Section 7 discusses the Q'_{\star} constraints obtained. We conclude in Section 8.

2 TIDAL EVOLUTION MODEL

We use an updated version of the publically available tidal evolution module **Planetary Orbital Evolution due to Tides** (POET hereafter; Penev et al. (2014)) to simulate the stellar and orbital evolution under the effects of tides. POET follows stellar evolution by interpolating among a grid of evolutionary tracks calculated using MESA (Paxton et al. 2011). MESA splits the star into many concentric shells, but for the purposes of POET, those are combined into two zones to track stellar evolution: convective envelope and radiative core. The two zones are assumed to have solid body rotation but are allowed to spin differently. They are also assumed to converge toward synchronous rotation on what is referred to as the core-envelope coupling timescale (Irwin et al. 2007; Gallet, F. & Bouvier, J. 2013), as well as exchange mass (which carries with it its specific angular momentum). The core-envelope coupling torques are calculated as:

$$\mathbf{T}_{\text{conv,c-e}} = -\mathbf{T}_{\text{rad,c-e}} = \frac{I_{\text{conv}}\mathbf{L}_{\text{rad}} - I_{\text{rad}}\mathbf{L}_{\text{conv}}}{(I_{\text{conv}} + I_{\text{rad}})\tau_{\text{c-e}}} - \frac{2L_{\text{conv}}}{3I_{\text{conv}}}R_{\text{rad}}^2\dot{M}_{\text{rad}} \quad (2)$$

where $I_{\text{rad/conv}}$ and $\mathbf{L}_{\text{rad/conv}}$ are the moment of inertia and the angular momentum vector of the core and envelope respectively, M_{rad} and R_{rad} are the mass and radius of the radiative core.

In addition to the change in internal structure, the angular velocity of the convective surface of stars is also effected by the torques exerted by stellar winds. The external torque leads to spin-down of the star at later stages of evolution (Schatzman 1962; Soderblom 2010; Gallet, F. & Bouvier, J. 2013; Gallet & Bouvier 2015). To account for this spin-down POET adopts a generalized formalism for the rate of angular momentum loss by assuming winds apply torque to the convective zone in direction opposite to \mathbf{L}_{conv} with a magnitude:

$$T_{\text{conv,wind}} \equiv K\omega_{\text{conv}}\min(\omega_{\text{conv}}, \omega_{\text{sat}})^2 \left(\frac{R_{\star}}{R_{\odot}}\right)^{1/2} \left(\frac{M_{\star}}{M_{\odot}}\right)^{-1/2} \quad (3)$$

where K is the parameterized wind strength, ω_{conv} is the angular

frequency of the convective envelope, ω_{sat} is the frequency above which the magnetic braking saturates, M_\star and R_\star are the mass and radius of the star, and M_\odot and R_\odot are the present day mass and radius of the Sun.

The orbital evolution model in POET is formulated in terms of the equilibrium tide model, but as already pointed out in the introduction, dynamical tide models can be incorporated by finding an effective phase lag. The prescription is based on the formalism of Lai (2012), but expanded to account for eccentricity. In summary,

(i) The quadrupole moment of the tidal potential in a spherical (ζ, θ, ϕ) -coordinate system is:

$$U(\mathbf{r}, t) = - \sum_{m, m'} U_{m, m'} \zeta^2 Y_{2, m}(\theta, \phi) \frac{a^3}{r^3(t)} \exp[-im' \Delta\phi(t)] \quad (4)$$

where a is the semi-major axis and $r(t)$ is the distance between the centers of the two objects at an arbitrary point on the orbit. $U_{mm'}$ are the coefficients of the spherical harmonics.

(ii) A Fourier series expansion is used to include effects of eccentric orbits:

$$\frac{a^3}{r^3(t)} \exp[-im' \Delta\phi(t)] = \sum_s p_{m', s} \exp(-is\Omega t) \quad (5)$$

with the $p_{m', s}$ coefficients pre-calculated as a function of eccentricity up to $s = 400$ to allow for even extreme orbital eccentricities. At $e=0.9$, truncating the tidal potential expansion to $s = 200$ is accurate to better than 1 part in 10^5 . We doubled the maximum s value for the sake of caution.

(iii) Following the equilibrium theory of tides, the effects of tidal dissipation are introduced as a lag in the response of the fluid perturbation inside the star. Each (ms) -component of the tidal potential has a distinct tidal frequency ($\tilde{\omega}_{m, s} = s\Omega - m\Omega_s$) and thus a distinct tidal lag. The Eulerian density perturbation and Lagrangian displacement is given as:

$$\xi_{m, s}(\mathbf{r}, t) = \frac{U_{m, s}}{\omega_0^2} \bar{\xi}_{m, s}(\mathbf{r}) \exp(-is\Omega t + i\Delta_{m, s}) \quad (6)$$

$$\delta\rho_{m, s}(\mathbf{r}, t) = \frac{U_{m, s}}{\omega_0^2} \delta\bar{\rho}_{m, s}(\mathbf{r}) \exp(-is\Omega t + i\Delta_{m, s}) \quad (7)$$

where $\delta\bar{\rho}_{m, s} = -\nabla(\rho\bar{\xi}_{m, s})$ and $\omega_0 \equiv \sqrt{GM/R^3}$ is the dynamical frequency of the primary star in the binary system.

(iv) The individual (ms) -component of the tidal torque and rate of dissipation of energy are calculated as:

$$\mathbf{T}_{m, s} = \int d^3x \delta\rho_{m, s}(\mathbf{r}, t) \mathbf{r} \times [-\nabla U^*(\mathbf{r}, t)] \quad (8)$$

$$\dot{E}_{m, s} = \int d^3x \rho_{m, s}(\mathbf{r}) \frac{\partial \xi_{m, s}(\mathbf{r}, t)}{\partial t} [-\nabla U^*(\mathbf{r}, t)] \quad (9)$$

(v) The evolution of the orbital parameters (semi-major axis a , eccentricity e , angle between spin angular momentum and orbital angular momentum vectors θ , and angular frequency of primary star ω) in terms of torque, energy, and angular momentum is calculated using the following equations:

$$\dot{a} = a \frac{-\dot{E}}{E} \quad (10)$$

$$\dot{e} = \frac{2(\dot{E}L + 2E\dot{L})L(M + M')}{G(MM')^3} \quad (11)$$

$$\dot{\theta} = \frac{(T_z - \tilde{T}_z) \sin \theta}{L} - \frac{(T_x - \tilde{T}_x) \cos \theta}{L} - \frac{T_x + \mathcal{T}_x}{S} \quad (12)$$

$$\dot{\omega} = \frac{(T_y + \mathcal{T}_y) \cos \theta}{L \sin \theta} + \frac{T_y + \mathcal{T}_y}{S \sin \theta} \quad (13)$$

where M is the mass of tidally distorted star, M' is the mass of the companion raising the tides, T_x, T_y, T_z are the components of tidal torque along x, y, z -directions, $\mathcal{T}_x, \mathcal{T}_y, \mathcal{T}_z$ are the non-tidal torques (i.e. stellar wind and core-envelope coupling), and $\tilde{T}_x, \tilde{T}_y, \tilde{T}_z$ are the tidal torques on the orbit due to other zones. The contribution of both stars to the orbital evolution is included.

The relation between the tidal quality factor and the phase lag is:

$$Q'_\star = \frac{15}{16\pi\Delta'_\star} \quad (14)$$

The tidal lag introduced in the above method allows for an arbitrary parameterization of tidal dissipation depending on the model being studied. For equilibrium tide models with constant phase lag, Q'_\star has a fixed value, while for dynamical tide models or variable phase lag equilibrium models, Q'_\star will in general depend on the orbital and stellar properties, as well as the particular tidal potential term being dissipated. In this work, we restrict our investigation to stars with similar internal structure, and only allow for a dependence on tidal frequency.

3 INPUT DATA

Stellar Rotational Periods

We wish to infer the parameters of the Q'_\star model using the observed rotation period of the primary star in binary star systems. We model the spin of the star as a Gaussian distribution whose mean and standard deviation are estimated as described below.

Lurie et al. (2017) performed an extensive study of the light curves of the eclipsing binaries available in the *Kepler Eclipsing Binary Catalog* and estimated the rotation period of the primary stars showing starspot modulations of their brightness.

The authors analyzed data available from *Kepler* Data release 25 in quarters 0-17. The Presearch Data Conditioning (PDC) pipeline suppresses stellar variability with $P \gtrsim 20$ days. Hence, rotation periods are available only for stars with $P < 20$ days.

The morphology of stellar variability for single stars is a well-modeled phenomenon. The authors use the out-of-eclipse region of the light curves to analyze the variability of stars in eclipsing binaries. Depending on the variations, they classify the light curves into six categories by visual inspection: starspot modulations, ellipsoidal modulations, pulsations, other periodic variability (do not belong to previous three or unidentified Heartbeat stars), non-periodic out-of-eclipse (flat-light curves or long-term smooth variation due to instrumental artifacts) and not eclipsing binary (lack of clear eclipses). Out of these, only starspot modulations can provide information about the rotation period of the stars. Starspot modulations are quasi-sinusoidal, with differential rotation and the formation and dissipation of starspots introducing long-term modulation (Davenport et al.

2015). The authors identify 816 eclipsing binaries that show such variations.

Two common ways to detect periodicity of variability in a time-variable signal are auto-correlation function (ACF) and Lomb-Scargle Periodogram (Lomb 1976). Following McQuillan et al. (2013), Lurie et al. (2017) identifies an initial rotation period for each binary using ACF. Since ACF is not sensitive to multiple rotation period peaks in the light curve signal, it can only serve as a validation for signals with multiple periods present due to the differential rotation of the star. For this purpose, the authors turn to Lomb-Scargle Periodograms in order to detect more than one peak of periodic variability in the out-of-eclipse light curves using a procedure by Rappaport et al. (2014), with ACF used for validation.

From the Lomb-Scargle Periodogram, the authors identified the two most significant peaks, imposing a threshold that peaks must be at least 30% of the highest peak. Each peak is then classified into two groups. Lowering this threshold results in the detection of spurious signals which might not be related to stellar variability. A window of frequency is selected for each group by selecting the local minima in a smooth periodogram on the right and left of the dominant peak. Inside this window, they again use the same threshold to identify the next dominant subpeak. Hence, for each system, there are a maximum of four possible solutions for the rotation period. Table 2 of Lurie et al. (2017) shows the periods and their respective peak height along with the period and peak height detected by the ACF. The ACF period comes closest to the most dominant peak in the periodogram.

As the authors themselves mention, the rotation period corresponding to the highest peak obtained in the first group ($P_{1 \min}$ in Table 2 of Lurie et al. (2017)) will be the closest to the equatorial rotation period. We adopt this as the nominal value of the rotation period of the primary star in our analysis. To obtain the uncertainty on the rotation period, we select the rotation period corresponding to the subpeak in the same group ($P_{1 \max}$ in Table 2 of Lurie et al. (2017)) and calculate the difference between $P_{1 \max}$ and $P_{1 \min}$. See Sec. 6.2 for an additional consideration we apply to account for the possibility that this procedure may under-estimate the rotational period uncertainty.

Binary Parameters

Windemuth et al. (2019) (W19 from now on) inferred the values of orbital and stellar parameters for detached eclipsing binaries in the *Kepler* field from the available photometric data. The authors selected 2877 eclipsing and ellipsoidal binaries available in the Villanova *Kepler* EB Catalogue (Prsa et al. 2011; Kirk et al. 2016). In order to get a catalog of well constrained detached eclipsing binaries, they first selected binaries with eclipse depths for the primary and secondary stars to be $> 5\%$ and $> 0.1\%$ of the normalized flux to ensure high signal to noise ratio. Next, they used the morphology parameter, provided by VKEBC, as $\text{morph} < 0.6$ to ensure the binaries in the sample are detached. The morphology parameter is based on a scheme that classifies light curves based on the type of binary star observed. Low values of this parameter correspond to a well-detached binary exhibiting clear separation between the eclipses, while higher values correspond to over-contact binary systems with sinusoidal variations (Matijević et al. 2012).

The orbital parameters and the stellar parameters of these systems are inferred by performing a simultaneous fit for the Light Curve (LC) and the Spectral Energy Distribution (SED). The observational uncertainties are then propagated to the model parameters using MCMC simulations with a likelihood function based on how well the LC, SED, extinction and distance are simultaneously reproduced.

Table 1. The maximum likelihood parameters of the binary systems used in this analysis and their spins.

KIC	$M_1 [M_\odot]$	$M_2 [M_\odot]$	$e \sin \omega$	$e \cos \omega$	$P_{\text{orb}} [\text{days}]$	P_* [days]	$\sigma_{P_*} [\text{days}]$
6962018	0.75	0.69	0.0002	0.00024	1.27	1.3	0.003
11616200	1.16	0.67	-0.014	0.00019	1.72	1.7	0.003
7798259	0.73	0.60	-0.039	7.6e-07	1.73	1.7	0.019
4380283	1.01	0.88	-4.9e-06	7.8e-05	1.74	1.7	0.003
7732791	0.64	0.65	0.039	0.00025	2.06	2.0	0.021
4579321	0.81	0.61	-0.03	-8.6e-05	2.11	2.1	0.03
11200773	1.09	0.42	-0.2	0.00037	2.49	2.5	0.033
9656543	0.79	0.76	-0.0041	8.4e-05	2.54	2.5	0.13
3834364	1.03	0.51	-0.15	0.00025	2.91	2.9	0.025
11228612	0.99	0.70	0.0044	4.2e-05	2.98	2.9	0.007
6312521	1.02	0.76	-0.091	0.00016	3.02	3.0	0.045
10960995	0.94	0.83	-5.9e-08	1.2e-07	3.12	3.0	0.11
11147276	1.18	0.89	-0.021	-6e-06	3.13	3.1	0.054
10091257	1.00	1.06	0.021	1.4e-05	3.4	3.3	0.06
6525196	0.91	0.85	-5.4e-05	4.7e-05	3.42	3.3	0.085
5022440	1.10	0.73	4.7e-07	-1.1e-06	3.69	3.6	0.13
5802470	1.13	0.77	2.7e-06	2.2e-05	3.79	3.8	0.073
4815612	1.17	1.00	-5.3e-08	-1.6e-07	3.86	3.7	0.083
3241344	1.01	0.51	-0.0055	-0.0041	3.91	3.9	0.014
11403216	1.07	0.45	-0.036	0.00034	4.05	4.0	0.019
10935310	0.84	0.54	0.17	-0.0018	4.13	3.9	0.014
10031409	1.16	1.11	0.004	6e-06	4.14	4.0	0.17
7838639	1.21	1.08	-0.0084	9.2e-06	4.23	4.1	0.081
3973504	0.88	0.57	-0.1	-4.9e-05	4.32	4.3	0.032
8957954	1.03	1.01	-2.5e-08	-1.9e-08	4.36	4.3	0.086
11252617	0.88	0.47	0.24	3.6e-05	4.48	4.5	0.05
4285087	0.99	0.97	-2e-05	-5.5e-05	4.49	4.5	0.049
4346875	0.94	0.55	-0.022	-9.8e-06	4.69	4.8	0.11
4947726	1.14	0.53	-0.15	0.079	4.73	4.4	0.21
11233911	0.84	0.94	0.016	0.00018	4.96	4.8	0.076
12004679	0.92	0.88	-0.0093	0.0018	5.04	5.6	0.21
2860788	1.03	0.83	-0.0045	-6.1e-06	5.26	5.0	0.084
9971475	1.10	0.80	-0.00033	4.6e-05	5.36	2.0	0.012
5730394	1.17	0.95	-0.019	-0.00025	5.52	6.3	0.38
5181455	0.96	0.54	-1.7e-06	-3.6e-07	5.58	5.5	0.11
8381592	1.01	0.73	-0.064	-0.0044	5.78	5.7	0.088
8618226	1.08	0.70	1.5e-05	0.0002	5.88	6.0	0.25
3838496	0.99	1.07	-0.0056	0.00079	5.98	5.7	0.061
10385682	1.00	0.99	-0.015	-5.9e-06	6.21	6.1	0.048
8580438	0.98	0.43	0.00062	0.002	6.5	7.5	0.19
10965963	1.08	1.00	0.045	-0.036	6.64	6.2	0.41
8746310	0.80	0.47	-2.5e-06	6.7e-05	6.86	8.3	0.4
7362852	1.16	1.11	0.0036	-0.0015	7.04	7.1	0.24
8543278	0.82	0.71	0.023	0.013	7.55	8.6	0.51
6927629	1.08	0.97	1.4e-05	2.7e-05	7.74	8.9	0.27
8364119	0.92	0.88	0.016	0.018	7.74	9.0	0.22
6949550	0.88	0.88	-0.011	-0.26	7.84	6.9	0.39
3348093	0.65	0.68	0.26	0.0069	7.96	8.2	0.27
9532123	0.99	0.75	-0.097	-0.21	8.21	7.3	0.37
9892471	0.91	0.56	-0.013	-0.00029	8.27	9.4	0.29
7816680	1.18	0.96	-0.018	1.9e-05	8.59	11.1	0.21
11391181	0.87	0.82	0.077	0.17	8.62	7.9	0.28
4839180	1.08	0.86	-0.0021	-0.0025	8.85	11.0	1.3
5652260	0.88	0.74	0.001	0.0012	8.93	11.0	1.2
11232745	0.73	0.65	3.6e-08	-3.9e-08	9.63	12.7	0.75
8984706	1.04	1.03	-0.013	0.015	10.1	12.5	1.3
5393558	0.92	1.04	0.23	-0.023	10.2	9.4	0.48
9353182	1.14	0.57	-0.042	0.036	10.5	10.5	0.22
4352168	1.03	0.73	-0.15	-0.15	10.6	10.2	0.6
7336754	1.14	0.73	0.016	0.012	12.2	13.2	1
6029130	0.92	0.87	0.0099	0.011	12.6	17.3	0.33
5871918	0.67	0.47	-0.32	-0.15	12.6	12.4	0.16
11704044	0.84	0.82	1e-06	2.7e-06	13.8	19.4	1.1
6359798	0.86	0.79	0.079	-0.41	14.2	3.4	0.029
10936427	1.08	1.12	-0.0074	0.0016	14.4	16.6	1.1
4678171	0.68	0.59	0.0025	-0.0035	15.3	20.3	5.4
7987749	0.90	0.79	0.043	-0.14	17	17.5	0.45
8356054	0.77	0.71	0.37	0.027	17.1	16.7	2.3
10330495	1.03	0.52	-0.056	-0.04	18.1	21.1	2.3
10992733	0.94	0.83	0.17	0.34	18.5	15.6	0.27
10711913	0.88	0.76	0.28	-0.077	19.4	18.6	1.1
4252226	0.99	0.92	0.13	-0.47	21.9	11.9	0.76
10215422	1.12	0.72	0.0014	0.29	24.8	24.8	2.2
4773155	1.03	0.95	-0.36	0.26	25.7	19.0	2

The authors performed this fit for 22 parameters. For our analyses, only the following parameters are of interest:

- Sum of masses of the primary and secondary star (M_{sum})
- Ratio of secondary mass to the primary mass (q)
- Age of the system (τ)
- Metallicity ($[\text{Fe}/\text{H}]$), assumed to be the same for both stars
- Eccentricity components of the orbit ($e \cos \omega$, $e \sin \omega$).

W19 provided posterior samples for 728 binaries. We restrict this sample further. First, since our analysis relies on the spin period

of the primary star, we perform a cross-match between these 728 binaries and binaries available in [Lurie et al. \(2017\)](#). We also apply limits on the stellar masses and metallicity ($0.4M_\odot < M_\star < 1.2M_\odot$ and $-1.014 < [\text{Fe}/\text{H}] < 0.537$), which further reduced our dataset. The mass limits were imposed to select only stars that have similar main sequence internal structure to the Sun, namely a significant convective outer shell, but not fully convective. The metallicity limits are driven by limitations imposed by POET, which at the moment is only capable of interpolating the stellar evolution within these mass and metallicity limits. Finally, we require reasonable orbital eccentricity $e < 0.8$ and orbital period of no more than 20 days.

Our final dataset contains 70 binary systems. We use the publicly available thinned posterior samples for our parameters of interest as observed probability distributions for Bayesian analysis. [Table 1](#) gives the maximum likelihood values (as reported by W19) of the mass of the primary star (M_1), mass of the secondary star (M_2), and eccentricity components of the orbit ($e \sin \omega$, $e \cos \omega$), along with the orbital period of the system, rotation period of the primary star and the 1σ -uncertainty assumed for the spin period (see [Sec. 3](#)). Note that for each binary only a single spin period is measured, which we assume is that of the primary (brighter) star.

4 Q'_\star FORMALISM

In this work, we assume that the tidal dissipation occurs only in the convective zones of the stars, meaning that we assume the tidal torque is applied only to the convective zone, with the core spin affected only indirectly through the core-envelope coupling. As mentioned in [Section 1](#), the effects of the binary system parameters on tidal dissipation can be studied by using a suitable parameterization for the tidal lag, $\Delta_{m,m'}$ or the corresponding tidal quality factor, $Q'_{m,m'}$, such that it can capture the orbital dynamics of the system under the effects of tides.

As discussed in [Sec. 2](#), we allow each Fourier component of the tidal potential to experience its own effective lag. In this work, we restrict the possibilities to some extent, by assuming that $\Delta'_{m,m'}$ depends solely on the tidal frequency (Eq. 1). Each equilibrium or dynamical tidal model predicts a different frequency dependence. In this work, we further simplify the prescription to assume that $\Delta_{m,m'}$ has a power-law dependence, on $\Omega_{\text{tide}} = m\Omega_{\text{orbit}} - m'\Omega_\star$. Furthermore, in order to avoid clearly non-physical and numerically unstable behavior occurring if $\Delta_{m,m'} \rightarrow \infty$, we assume the dissipation saturates to some maximum value:

$$\Delta'_{m,m'} = \text{sign}(\Omega_{m,m'})\Delta_0 \min \left[1, \left| \frac{\Omega_{m,m'}}{\Omega_{\text{break}}} \right|^\alpha \right] \quad (15)$$

or in terms of Q'_\star :

$$Q'_{m,m'} = \text{sign}(P_{m,m'})Q_0 \max \left[1, \left| \frac{P_{m,m'}}{P_{\text{break}}} \right|^\alpha \right] \quad (16)$$

where α is the powerlaw index parametrizing the frequency dependence, $\Delta_0 = \frac{15}{16\pi Q_0}$ parametrizes the maximum allowed dissipation, $\Omega_{m,m'} = \frac{2\pi}{P_{m,m'}}$ is the tidal frequency of a particular tidal wave, and $\Omega_{\text{break}} = \frac{2\pi}{P_{\text{break}}}$ is the frequency at which the dissipation saturates. See [Appendix A](#) for a small modification we introduce, which improves numerical performance without significantly changing the evolution.

We now wish to find constraints on Q_0 , α , and P_{break} that can simultaneously reproduce the observed spins of the primary stars in all the binaries in our input sample. In practice, the tidal effects on the spin of each binary will be dominated by a narrow range

Table 2. The parameters sampled during MCMC and their priors. The W19 joint prior is constructed using KDE from the W19 MCMC samples.

Parameter	Units	Description	Prior
M_1	M_\odot	Mass of the primary star	W19
M_2	M_\odot	Mass of the secondary star	W19
$[\frac{\text{Fe}}{\text{H}}]$	-	Metallicity of both stars	W19
τ	Gyr	Age of the system	W19
e	-	Present day eccentricity of the Orbit	W19
$P_{\star,\text{init}}$	days	Initial spin period of the stars	$U()$
$\log_{10} Q_0$	-	Dissipation parameter. See Eq. 16	$U(5, 10)$
α	-	Dissipation parameter. See Eq. 16	$U(-5, 5)$
$\log P_{\text{break}}$	rad/day	Dissipation parameter. See Eq. 16	$U(\log 0.5 d, \log 50 d)$

of frequencies, so for a given binary, we will be able to constrain $Q'_{m,m'}$ for a narrow range of periods. Furthermore, because tides get weaker as the separation between the two stars increases, we expect that for the lowest periods of our sample of binaries all systems will be synchronized, thus providing only a lower limit on the dissipation (upper limit on Q'_\star), while at the longest periods stellar spins will not be significantly affected by tides, providing only an upper limit to the dissipation (lower limit on Q'_\star). Because the effects of tides decrease very precipitously as the orbit gets wider, there should be only a small number of binaries in between these two regimes providing two-sided constraints. It should be noted that the range of orbital periods with asynchronous binaries whose spin is nonetheless significantly affected by tides is much wider than one may naively expect. This is caused by the fact that the rate at which stars lose angular momentum due to magnetized winds scales as the cube of the angular velocity. Hence, maintaining synchronous rotation requires ever stronger tidal coupling as the orbital period decreases. Even with that, however, combining the constraints from multiple binary systems is required to get a measurement of the tidal dissipation and detect any potential frequency-dependence.

5 BAYESIAN ANALYSIS

We use the Markov Chain Monte Carlo algorithm as implemented in the Python package [emcee \(Foreman-Mackey et al. 2013\)](#). [emcee](#) is based on a class of ensemble sampler algorithms that uses affine invariant transformation as a proposal function to simultaneously advance multiple not-independent chains, referred to as walkers, in the parameter space. We refer the reader to ([Foreman-Mackey et al. 2013](#)) and references therein for details of the algorithm.

The choice of the number of walkers is a compromise between parallelization efficiency and the need to accumulate a sufficient number of steps to ensure the distribution of samples has converged to the target posterior. For our analysis, we use 64 walkers for each binary to sample the 9-dimensional space of parameters required to calculate the orbital evolution.

The parameters sampled by MCMC and their respective priors are listed in [Table 2](#). For the physical parameters of the binaries we construct a joint prior using Kernel density estimation from the MCMC samples published by W19, and for the dissipation parameters we use very broad uniform priors.

5.1 Prior Transformation

Because the prior distributions built from W19 samples are quite complex structures in a multi-dimensional space, the MCMC sampling becomes very inefficient. In order to remedy this situation, instead of directly sampling from the prior distribution of the parameters from [Table 2](#), we use a transformed set of parameters (u_i with

$i = 1 \dots 9$) such that each of those has an independent prior distribution uniformly distributed between 0 and 1. Given a sample of values for u_i , the physical and dissipation parameters required to calculate the evolution are then found by applying a prior transformation. This procedure dramatically simplifies the posterior likelihood the MCMC process must sample from, making it directly proportional to the likelihood that the actual spin of the primary star as observed today is equal to the spin period predicted by the evolution assuming the given parameters.

The joint prior distribution we wish to impose on the physical parameters of each binary (the first 5 parameters listed in Table 2) is the posterior distribution W19 samples are drawn from. We start by isolating only the parameters we need. For each sample, we combine the components of eccentricities ($e \cos \omega$ and $e \sin \omega$) to just eccentricity ($e = \sqrt{(e \cos \omega)^2 + (e \sin \omega)^2}$). We then construct a marginalized probability distribution function $\pi(M_{sum}, q, \tau, [\text{Fe}/\text{H}], e)$, where $M_{sum} \equiv M_1 + M_2$ and $q \equiv M_1/M_2$, using a Kernel density estimator (KDE) with a Gaussian kernel with a bandwidth determined using the improved Sheather-Jones algorithm (Botev et al. 2010).

Finally, W19 samples were generated assuming independent $U(0, 1)$ priors on $e \cos \omega$ and $e \sin \omega$. This has the undesirable effect that when converted to prior on eccentricity, the probability of $e = 0$ is zero, even if the cloud of points in $e \cos \omega, e \sin \omega$ space clearly includes the origin. This will propagate to the prior distribution we impose resulting in erroneously imposing an upper limit on the dissipation (lower limit on Q'_*) for such systems. To see this, consider a system for which the primary star is consistent with spinning synchronously with the orbit, and the $e \cos \omega, e \sin \omega$ cloud of points is centered on the origin (i.e. observations are consistent with circular orbit). We expect that for such a system arbitrarily small Q'_* should be acceptable since large amounts of tidal dissipation will predict a completely circularized and synchronized system. Instead, the prior on eccentricity imposed by W19 will exclude that configuration, erroneously requiring a small eccentricity comparable to the uncertainty in $e \sin \omega$ (the much less well constrained of the two components) to survive to the present day. Instead of the W19 prior, we wish to impose independent priors $e \in U(0, 1)$ and $\omega \in U(0, 2\pi)$. The desired prior is obtained from the W19 prior by simply dividing by e and re-normalizing.

To be precise, if the s^{th} W19 sample has values for the parameters given by $M_{sum} = M_s, q = q_s, \tau = \tau_s, [\text{Fe}/\text{H}] = [\text{Fe}/\text{H}]_s$, and $e = e_s$, the prior probability density of the systems parameters is given by:

$$\pi\left(M_{sum}, q, \tau, \left[\frac{\text{Fe}}{\text{H}}\right], e\right) \propto \sum_s k_M(M_{sum} - M_s) k_q(q - q_s) \times k_\tau(\tau - \tau_s) k_{[\text{Fe}/\text{H}]} \left(\left[\frac{\text{Fe}}{\text{H}}\right] - \left[\frac{\text{Fe}}{\text{H}}\right]_s \right) \frac{k_e(e - e_s)}{e} \quad (17)$$

where $k_M \dots$ are the kernels used for each of the quantities, and the factor of $1/e$ in the last term is responsible for changing the priors as explained above.

The resulting prior transformation converting u_1, \dots, u_5 for a given MCMC sample to the corresponding physical system parameters is then:

$$\begin{aligned} M_{sum} &= F_M^{-1}(u_1) \\ q_i &= F_q^{-1}(u_2 | M_{sum}) \\ \tau_i &= F_\tau^{-1}(u_3 | M_{sum}, q) \\ Z_i &= F_{[\text{Fe}/\text{H}]}^{-1}(u_4 | M_{sum}, q, \tau) \\ e_i &= F_e^{-1}(u_5 | M_{sum}, q, \tau, \left[\frac{\text{Fe}}{\text{H}}\right]) \end{aligned} \quad (18)$$

with

$$\begin{aligned} F_M(M) &\equiv \int_{-\infty}^M dM_{sum} \int_{-\infty}^{\infty} dq \int_{-\infty}^{\infty} d\tau \int_{-\infty}^{\infty} d\left[\frac{\text{Fe}}{\text{H}}\right] \int_{-\infty}^{\infty} de \\ &\quad \pi\left(M_{sum}, q, \tau, \left[\frac{\text{Fe}}{\text{H}}\right], e\right) \\ F_q(q | M_{sum}) &\equiv \int_{-\infty}^q dq' \int_{-\infty}^{\infty} d\tau \int_{-\infty}^{\infty} d\left[\frac{\text{Fe}}{\text{H}}\right] \int_{-\infty}^{\infty} de \\ &\quad \pi\left(M_{sum}, q', \tau, \left[\frac{\text{Fe}}{\text{H}}\right], e\right) \\ &\dots \end{aligned} \quad (19)$$

The above calculations are feasible because calculating multi-dimensional integrals is not necessary. Kernel functions are normalized, so integrals over $\pm\infty$ are all unity.

The priors on the dissipation parameters and the initial spin frequency of the primary star are assumed uniform. The corresponding prior transform for those is just a simple shift and scaling to match the limits.

The parameters not listed in Table 2 and required by the evolution (Sec. 2) are assumed constant with the following values:

$$\begin{aligned} K &= 0.17 M_\odot R_\odot^2 \text{ day}^2 \text{ rad}^{-2} \text{ Gyr}^{-1} \\ \omega_{sat} &= 2.45 \text{ rad day}^{-1} \\ \tau_{c-e} &= 5 \text{ Myr}. \end{aligned} \quad (20)$$

5.2 MCMC Convergence Diagnostic

The samples generated by an MCMC algorithm can be shown to follow the specified posterior distribution in the limit of infinitely long chains. Real-world applications then need to demonstrate that the generated chains are long enough to get a good approximation to the distribution. There are two concerns that must be addressed. First, in infinite chains the starting positions are irrelevant. In finite chains however, an MCMC process requires some number of steps before subsequent samples can be shown to come from the desired distribution to a good approximation. This is usually referred to as the burn-in period, and a typical practice is to discard the early samples. The second concern is that one needs a sufficient number of post-burn-in samples in order to estimate the targeted quantities with a desired precision.

In this work, we are interested in estimating quantiles of the posterior distribution. Raftery & Lewis (1991) derived diagnostics for single chain MCMC of a single quantity that answer the questions:

- What is the smallest N such that the probability that the $N + 1$ step in the chain is below some threshold value is within a specified precision of the limit of that probability for $N \rightarrow \infty$.
- What is the variance of the estimated value of the cumulative distribution at the threshold value from the MCMC chain after the N^{th} sample.

The Raftery & Lewis (1991) procedure cannot be directly applied to emcee chains because that involves multiple non-independent chains. In Patel & Penev (2022) and Penev & Schussler (2022) we adapted the Raftery & Lewis (1991) procedure for emcee chains, allowing us to estimate when enough samples have been generated

to reliably and precisely estimate a specified quantile of some target quantity.

In this work, we select a grid of tidal periods $P_{tide,i}$ and use the emcee samples of Q_0 , α , and P_{break} to evaluate the tidal model (Eq. 16) at each of these periods to obtain samples of $Q'_i = Q'_{m,m'}(P_{tide,i})$. For each of these quantities, we wish to find the 2.3%, 15.9%, 84.1%, and 97.7% quantiles. Using the adapted Raftery & Lewis (1991) formalism, we find a burn-in period for each Q'_i for each quantile, requiring that the fraction of the first post-burn-in samples of Q'_i (one for each walker) below the quantile is within 10^{-3} of the equilibrium probability, and estimate the uncertainty in the CDF for each Q'_i and quantile combination from the remaining samples after discarding the burn-in.

Because finding a given quantile requires knowing the burn-in period, and finding the burn-in period requires knowing the quantile, we iterate between the two to find a mutually consistent combination.

6 Q'_\star CONSTRAINTS

6.1 Individual Constraints

From the MCMC we obtain posterior samples for Q_0 , P_{break} and α for each system. These samples are converted to $Q'_\star(P_{tide})$ using Equation 16 evaluated at 30 separate tidal periods \log -uniformly spaced between 1 and 50 days. For each tidal period we apply the convergence diagnostics described in Section 5.2 to find the 2.3, 15.9, 84.1, and 97.7 percentiles of Q'_\star at that tidal period (corresponding to $\pm 1\sigma$ and $\pm 2\sigma$ uncertainties) together with the burn-in steps and cumulative distribution uncertainty.

Figures 1 and 2 show the KDE estimate of the posterior distribution of Q'_\star at each tidal period (color-coded heat map), the 2.3, 15.9, 84.1, and 97.7 percentiles (black dotted or solid curves), the 50th percentile as the thin horizontal red curve, and the orbital period (thick vertical black line). The solid parts of the quantile curves, delineated with vertical red lines, mark the range of periods for which the Q'_\star distribution and quantiles are reliable, i.e. dominated by the data rather than the priors and not affected by potentially under-estimated uncertainty of the spin (see Sec. 6.2 for details).

Figures 3 and 4 show the estimated burn-in periods (see Sec. 5.2) for the four quantiles of Q'_\star at each tidal period as the curves (solid corresponding to the reliable range of periods, dotted otherwise), as well as the total number of steps we accumulated for each system (black area). As that figure demonstrates, for the tidal periods where a given quantile is deemed reliable (see Sec. 6.2), for all our systems we have accumulated enough samples to move past the burn-in period.

Finally, Figures 5 and 6 show the estimated standard deviation of the cumulative distribution function (CDF) at each quantile estimated as described in Sec. 5.2 from the samples after burn-in is discarded.

Two-sided limits on Q'_\star

The systems for which we obtain two-sided limits significantly differ between the orbital period and the spin period of the primary star and significantly deviate from the spin period of an isolated star given the same mass and age. For example, in the case of KIC11232745, the orbital period of the system is 9.6 days, while the spin period is 12.7 days. The lower bound on Q'_\star comes from not allowing high dissipation, which would cause the primary star to synchronize with the orbit. The upper bound on Q'_\star is due to the requirement of minimal dissipation such that the tidal influence on the spin of the star is not negligible compared to the effect of stellar winds. Given the

very steep drop off of the effects of tides with orbital separation (tidal torque decreases as the fourth power of the orbital period), at first glance it may appear that such systems should be so rare that finding several in a sample of 70 binaries would be surprising. However, two-sided limits on Q'_\star correspond to stars with spin periods comparable (though not quite equal) to the orbital period. As a result, since stellar wind torques scale strongly with the spin period (third power of the spin period), which is itself related to the orbital period, the transition from fully synchronized systems to systems unaffected by tides is much more gradual than thinking about tides alone would predict.

Upper Limit on Q'_\star

There are systems where we only obtain an upper bound on $\log_{10} Q'_\star$ (lower bound on the dissipation). In these cases, the spin period of the primary star is synchronized with the orbit. Above this limit, the dissipation is not high enough to maintain a spin-orbit lock and keep the star synchronized with the orbit. However, reproducing the observed state of the system can tolerate arbitrarily large dissipation (arbitrarily small Q'_\star) since that will just result in the spin-orbit lock being achieved earlier.

Lower Limit on Q'_\star

Similarly, there are systems with only a lower bound on $\log_{10} Q'_\star$ (an upper bound on the dissipation). This limit is obtained for systems whose spins are consistent with that of isolated stars of similar mass and age. The inability to distinguish the spin from that of an isolated star is generally driven by the fact that the age is usually the least well constrained parameter. We stress that the non-tidal parameters we assume (core-envelope coupling timescale, wind strength, wind saturation frequency etc.) were tuned to reproduce the observed spins of isolated stars with well known ages (ones residing in open clusters). Hence, if we calculate the evolution of a binary under the assumption of $Q'_\star \rightarrow \infty$, the predicted spin of each star in the binary is the same as that of an isolated star with the same mass and age. The lower limit to Q'_\star produced by these systems is thus a statement that if the dissipation were any larger than this, it would have had a detectable effect on the spin.

For some systems, the lower bound on $\log_{10} Q'_\star$ can be due to eccentricity rather than the spin period of the primary star. It may be that the uncertainty in the age does not allow us to distinguish the spin from that of an isolated star, but if non-zero orbital eccentricity is detected with high significance, dissipation must be weak enough to avoid circularizing the system.

6.2 Reliable Portion of Individual Q'_\star Constraints

Examining the posterior distributions of $\log_{10} Q'_\star$ in Fig. 1 and 2, it is clear that each individual binary is sensitive to the dissipation only in a relatively narrow range of periods. For example, the difference between the median and the 97.7th percentile of the distribution has a sharp minimum. Sufficiently far away from that period, the increase of the 97.7th percentile is limited to large extent by the fact that we restrict the powerlaw index α in Eq. 16 to a maximum value of 5. Similarly, for some systems, the small quantiles peak at some period, and, away from that, the slope is limited by the assumption that $\alpha > 5$.

In order to select the region where constraints are dominated by the observed state of the binary rather than the priors, we evaluate the absolute difference between the highest/lowest quantiles and the

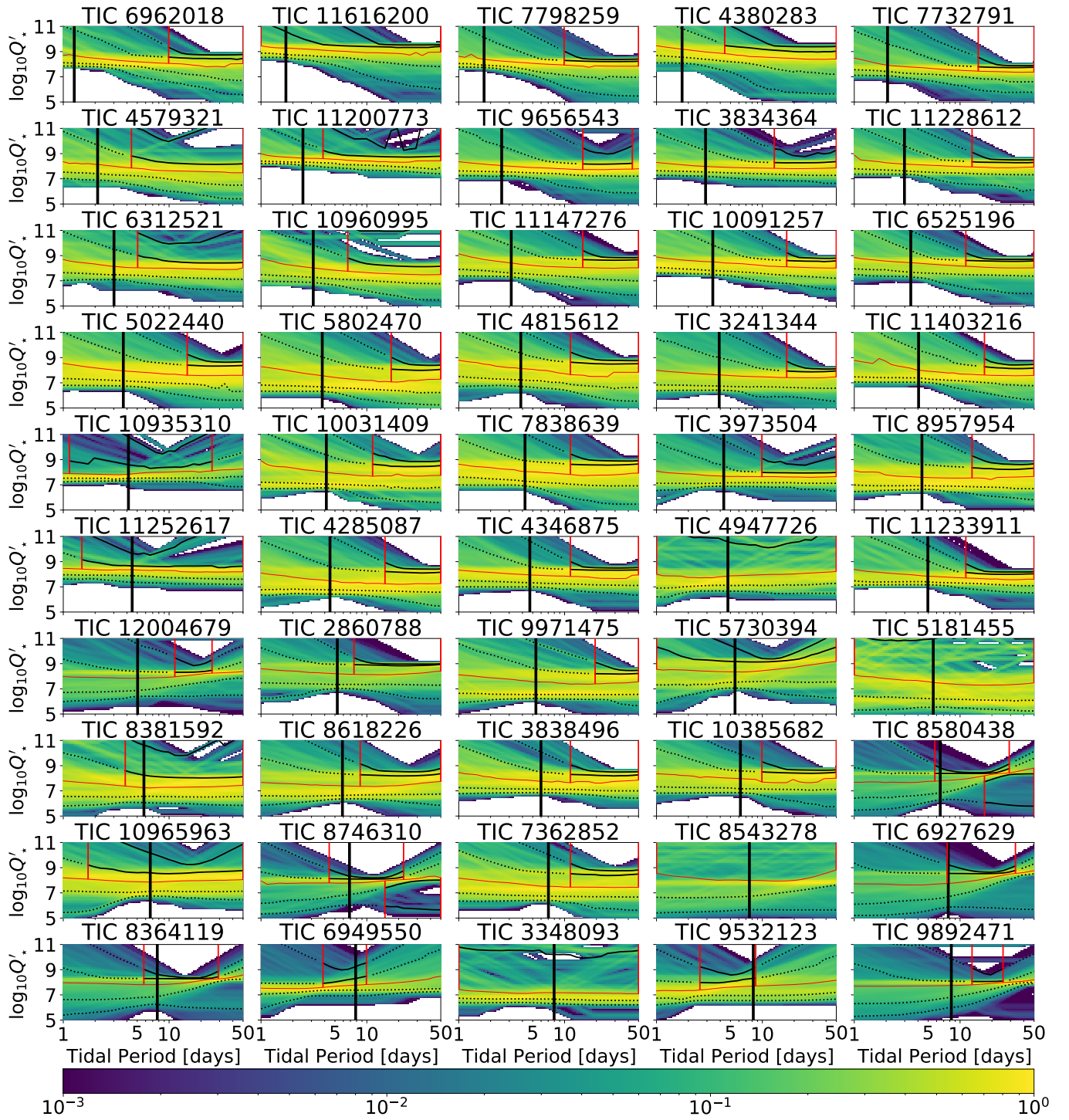


Figure 1. Individual constraints on $\log_{10} Q_*$ as function of tidal periods, $P_{tide} \in [0.5, 50]$ days for each binary systems. The color heat map represents the posterior probability density function of Q_* at each tidal period generated by evaluating Eq. 16 for each MCMC sample after the estimated burn-in period. The horizontal black lines show the 2.3, 15.9, 84.1, and 97.7 percentiles with solid line where we believe the constraints are reliable and dotted where we believe they are either significantly affected by our assumed priors, or may be affected by under-estimated uncertainty of the spin (see Sec. 6.2). The thick black vertical line shows the orbital period of the system, the thin red horizontal line is the median and vertical red lines delineate the range of periods outside of which the assumed priors could be significantly driving the constraints.

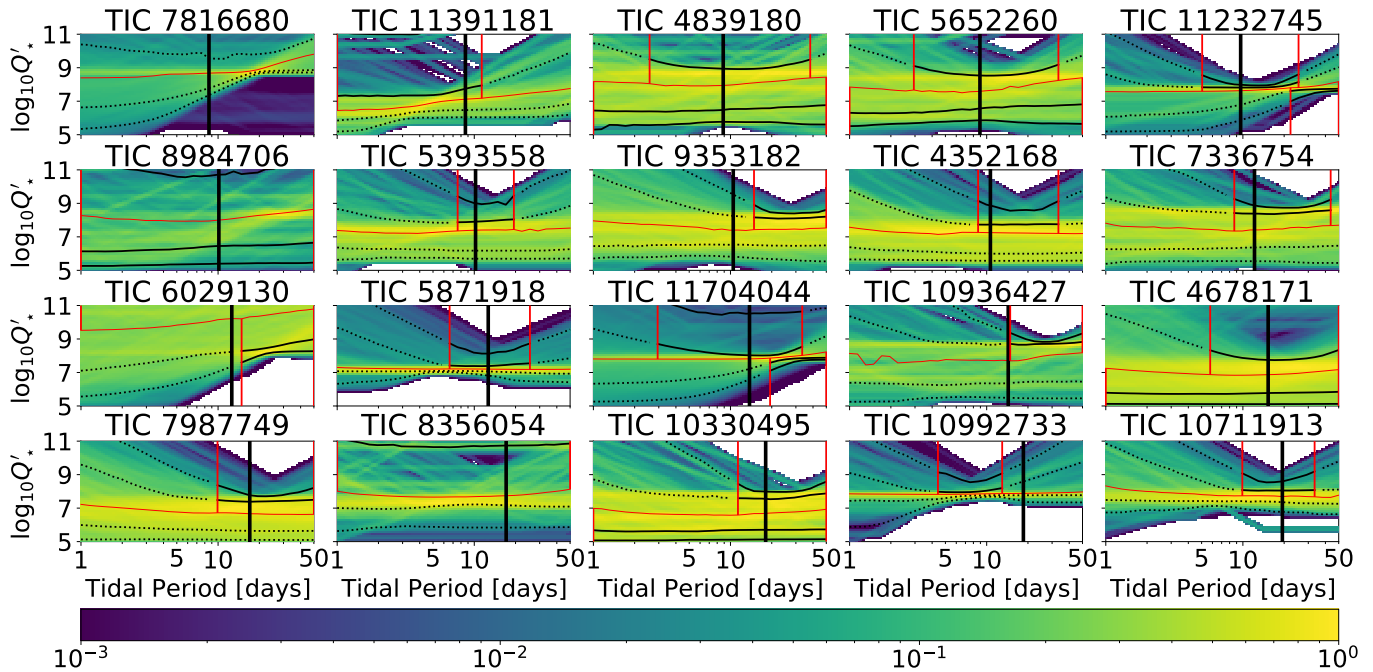


Figure 2. Same as Fig. 1 but for the remaining systems.

median at each tidal period. We then select the period range where this difference remains within 0.5 dex of its minimum value. The upper/lower half of the distribution is then only deemed reliable within that period range.

For the systems for which we obtain a lower bound or two-sided bound on $\log_{10} Q'_\star$, we must further examine the difference in the measured spin period and the orbital period. Generally, the statistical uncertainty in measuring the spin period is small compared to stellar differential rotation. As described in Sec. 3, we estimate that difference using the detection of multiple peaks in the Lomb-Scargle periodogram. However, if the star spots modulating the lightcurve of a particular star happen to all come from a narrow range of latitudes at the time they were observed, our approach will under-estimate the amount of differential rotation. The result could be a star which synchronized the spin to the orbit, but for which, due to differential rotation, the LC modulation happens to have a slightly different period and the difference appears significant because we under-estimate the amount of differential rotation. In turn, this will produce an upper limit to the dissipation (lower limit on Q'_\star) that is not justified by the observations. To compensate for this possibility, we trust only the upper limit to $\log_{10} Q'_\star$ our analysis gives for systems with measured spin periods within 17% of the measured orbital period (approximately the amount of differential rotation between the poles and equator of the Sun) and ignore the lower limit. Suggestively, the distribution of fractional difference between spin and orbital period for our systems has a gap between 17% and 21%, with most systems below 17%, perhaps hinting at a switch from a population of synchronized to non-synchronized systems, though the sample is not large enough to claim this is statistically significant or to explore possible explanations.

6.3 Combined Constraints

As expected, individual constraints are sensitive to a limited range of frequencies, and most binaries only produce upper or lower limits,

but only a few produce both. As a result, meaningful measurement of Q'_\star can only be obtained by combining the individual constraints. Furthermore, since we selected all our binaries to have similar internal structure, it is not unreasonable to assume they should have similar dissipation.

A common constraint, which agrees with all the constraints obtained by the individual binary systems, can be found by multiplying the posterior probability density functions of $Q'_\star(P_{\text{tide}})$ for the binary systems for each P_{tide} , obtained using KDE. This of course is complicated by the considerations described in Sec. 6.2. For a given system, at a given tidal period, we have already identified whether we trust both halves of the distribution, just the upper half, just the lower half, or neither. If neither side of the distribution is reliable, we simply do not include that system in the product for the given tidal period. If only one side of the distribution is reliable, we replace the unreliable part of the probability density with the probability density at the median and re-normalize before including the distribution in the product for the combined distribution.

One of our binaries – KIC 7816680 – produces constraints that are in conflict with the combined constraint from the other binaries for all tidal periods above 7 days. An outlier binary can have many explanations:

- (i) There may be additional objects in the system resulting in a very different orbital evolution than we calculate assuming just two objects
- (ii) A third object in the system or another star along the same line of sight could be contributing extra light to the system. Since W19 models the spectral energy distribution assuming just the two binary components that could shift the inferred properties of the binary.
- (iii) Spin period measurements sometimes detect an alias of the spin period, or perhaps the spot modulations come from the secondary star instead of the primary, invalidating our assumption that measured spin is that of the brighter star.
- (iv) The stellar evolution models used in the W19 analysis to find

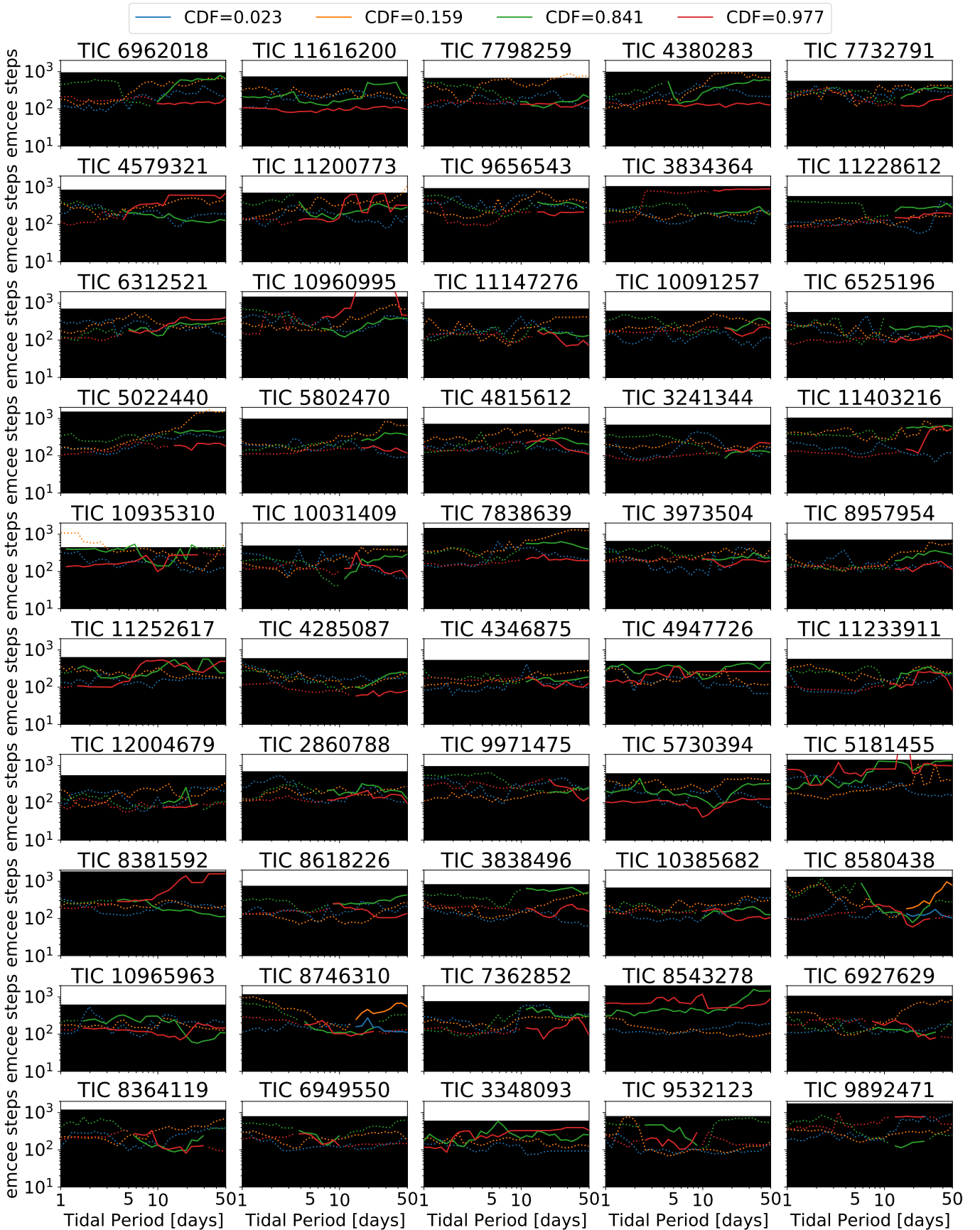


Figure 3. Estimated burn-in periods required for each of the percentiles of $\log_{10} Q'_*(P_{tide})$ at each tidal period (lines). Solid lines are used for the range of periods where the constraints are deemed reliable (Sec. 6.2), dotted outside this range. The black area shows the number of steps accumulated for each system.

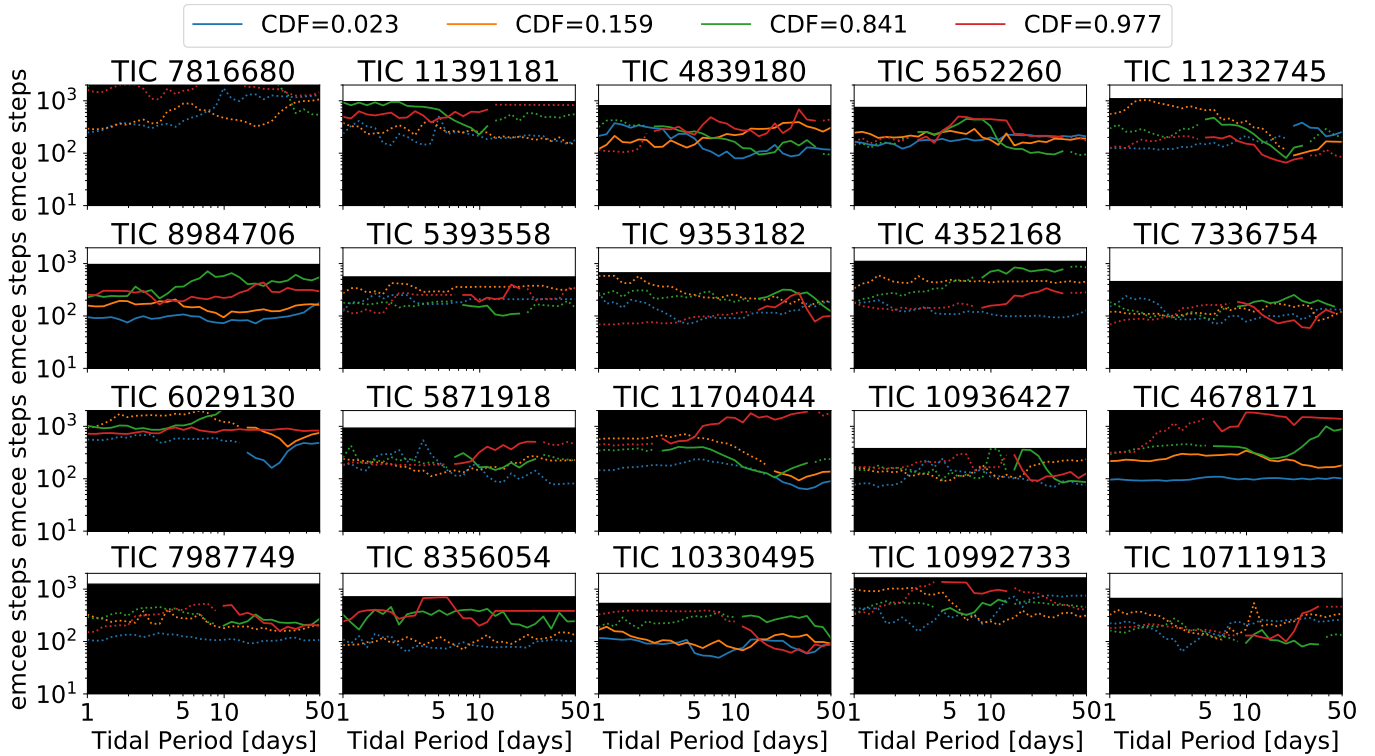


Figure 4. Same as Fig. 3 but for the remaining systems.

binary parameter distributions and in our orbital evolution calculations may not be applicable. In fact, W19 already report discrepancies for young stars and caution discrepancies are also expected for post-main-sequence stars, and POET stellar evolution interpolation is unreliable past the end of the main sequence as it was never designed to handle such stars.

We suspect KIC 7816680 falls in the final category. The primary star has a maximum likelihood mass of $1.2M_\odot$ and maximum likelihood age of 9.4 Gyr, hence the W19 model of this binary involves a post-MS primary, so some amount of difficulty with stellar evolution models is expected.

Fig. 7 shows the combined constraint on $\log_{10} Q'_\star$ obtained through the above procedure, excluding KIC 7816680.

An important question that must be considered is whether the combined constraints are indeed consistent with all individual constraints. After all, it is possible to multiply two mutually highly inconsistent distributions and obtain a combined constraint that is somewhere in the middle that is highly inconsistent with either distribution. Fig. 8 shows the 2.3, 15.9, 50.0, 84.1, and 97.7 percentiles of the combined constraints (same as the lines in Fig. 7) along with the 2.3 and 97.7 percentiles for each individual system at the tidal period where the distance between the 2.3 and 97.7 percentiles is smallest. As can be seen in Fig. 8, there is at least some overlap between the allowed $\log_{10} Q'_\star$ values for each system and the combined constraint. In other words, the combined constraint is capable of reproducing the observed spins of all the binaries in our sample except KIC 7816680.

7 DISCUSSION

7.1 Merging with Prior Results

Our group has embarked on a systematic effort to construct a comprehensive empirical picture of tidal dissipation in low mass stars by combining constraints derived from multiple tidal effects observable in multiple collections of binary star or exoplanet systems. We rely on a common approach of analyzing each system individually, employing Bayesian analysis to account for observational and model uncertainties, and combining the individual constraints to find a common prescription for Q'_\star capable of explaining the observed properties of each population of objects. We begin by placing this result in the context of the previous results from our group (Fig. 9).

The most closely related study by our group (Patel & Penev 2022) (PP22 from now on) analyzed the tidal effects on the spin of 41 of the Kepler eclipsing binaries analyzed here, but assuming $Q'_\star = \text{constant}$ and without the benefit of the W19 parameters, which were not available at the time. We used a similar approach, analyzing one binary at a time, and then combining the individual posterior distributions of Q'_\star for each binary system. We obtained a common constraint $Q'_\star = 7.82 \pm 0.035$, which was in agreement with each of the individual constraints. As can be seen from Fig. 9, there is also agreement with the results found by this study. That is of course expected, since many of the same binaries are analyzed both here and by (Patel & Penev 2022), though with less precise parameters and using a different prescription for Q'_\star .

Penev & Schussler (2022) (PS22 hereafter) studied tidal circularization of the single line spectroscopic binaries in three open clusters (M35, NGC 6819, and NGC 188) to obtain constraints of a frequency dependent Q'_\star . PS22 constructed an envelope in the period-eccentricity distribution for each cluster which encompasses all observed binary systems, and required that dissipation is strong enough

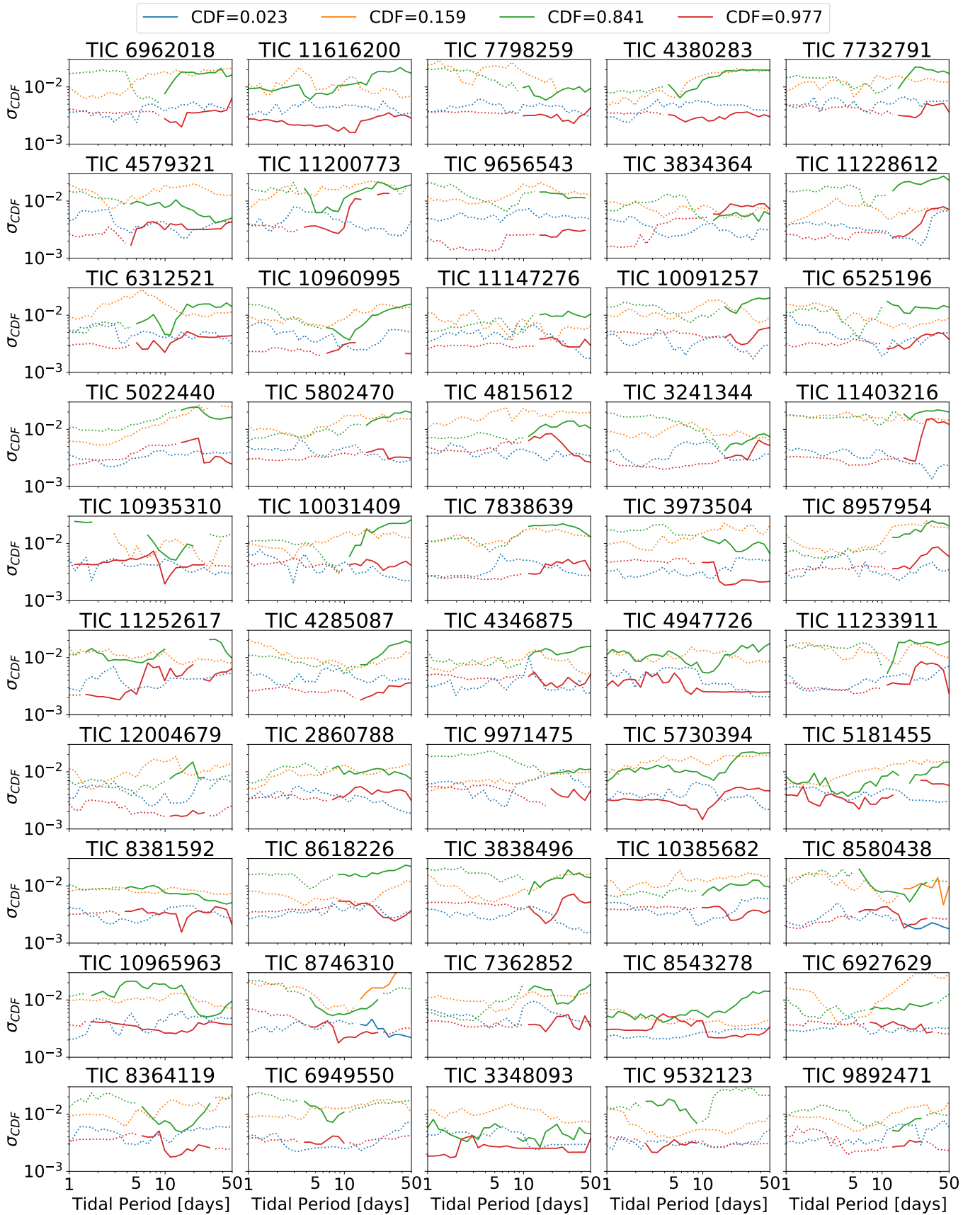


Figure 5. Estimated uncertainty (standard deviation) of the fraction of the distribution of $\log_{10} Q_{\star}(P_{\text{tide}})$ that lies below each quantile. Solid lines are used for the range of periods where the constrained are considered reliable (see Sec. 6.2), dotted lines otherwise.

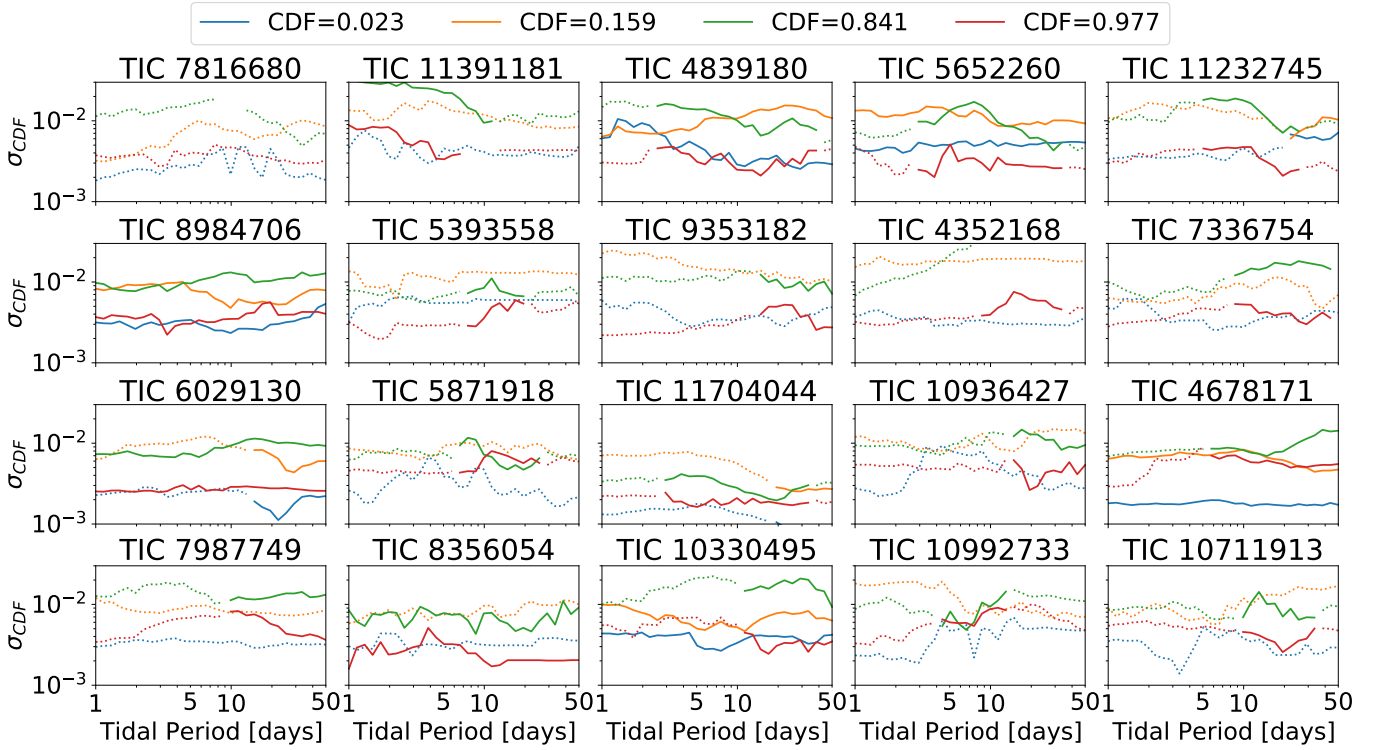


Figure 6. Same as Fig. 5 but for the remaining systems.

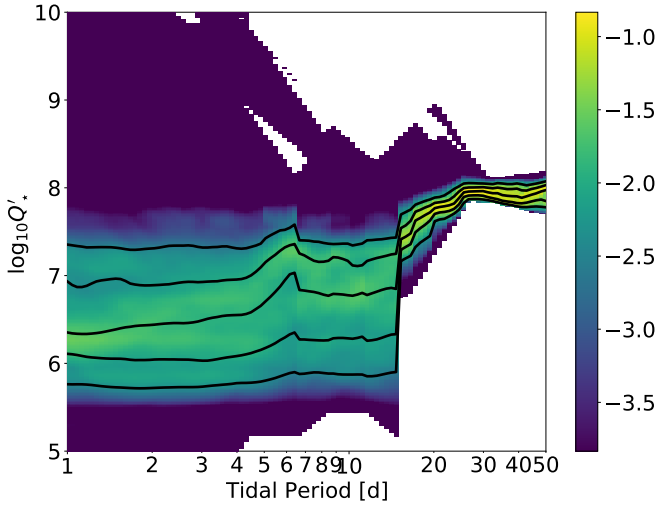


Figure 7. Combined constraints on Q'_\star as a function of tidal period, calculated by multiplying the probability distribution functions obtained for the individual binary system at each tidal period, after applying corrections per the discussion in Sec. 6.2. The black lines correspond to the 2.3, 15.9, 50.0, 84.1, and 97.7 percentiles of $\log_{10} Q'_\star$ constraints.

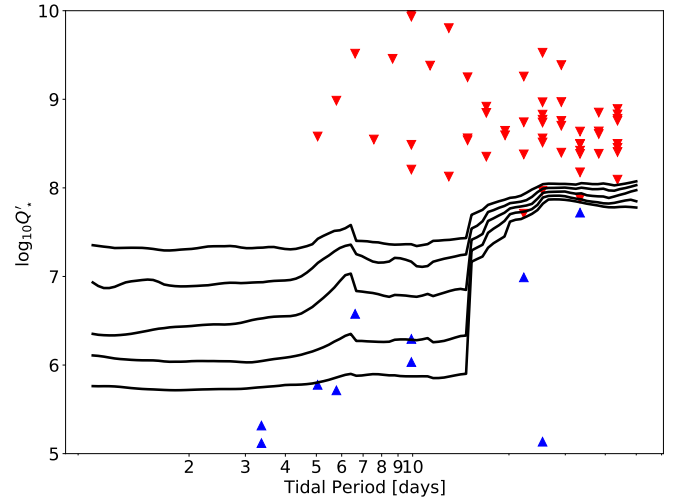


Figure 8. Comparison between the combined constraint and the individual constraints. The lines show the 2.3, 15.9, 50.0, 84.1, and 97.7 percentiles of the combined $\log_{10} Q'_\star$ constraints (same as in Fig. 7). The blue up and red down triangles show the 2.3 and 97.7 percentiles of the constraint for individual systems at the tidal period where the difference between the two is smallest.

to place any binary below the envelope and weak enough to allow reproducing the observed present day eccentricity of each system. Using the same formalism for frequency-dependent Q'_\star as defined in Equations 16, PS22 found that for the two older clusters (~ 2 Gyr old NGC 6819, and ~ 7 Gyr old NGC 188) $5.5 < \log_{10} Q'_\star < 6$ for $2 \text{ days} < P_{\text{tide}} < 10 \text{ days}$, while for the 150 Myr old M35 $\log_{10} Q'_\star < 4.6$. Outside the $2 \text{ days} < P_{\text{tide}} < 10 \text{ days}$ range the dissipation was not well constrained. The difference in tidal periods

probed by the two studies is due to the fact that much stronger tides are required to affect the orbit than the spin of the primary star.

Penev et al. (2018) (P18 from now on) investigated the effect of tides on the spin of exoplanet host stars. Thanks to their small mass, the tides planets produce on their parent stars are much weaker than binary star tides. As a result, studying exoplanet systems allows probing tidal dissipation at even shorter orbital (and hence tidal) periods than this or any of the above studies. P18 found a

[h!]

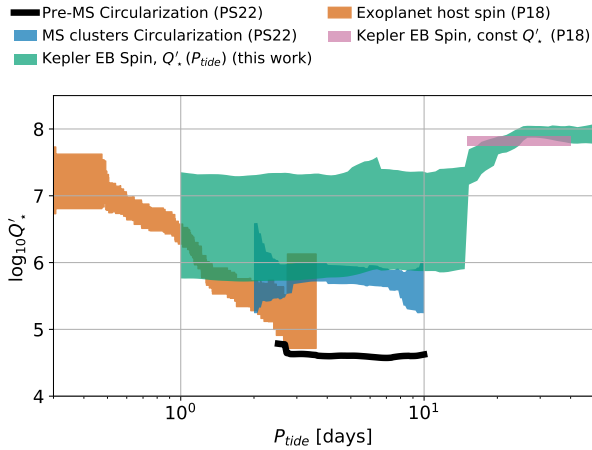


Figure 9. Constraints on tidal dissipation ($\log_{10} Q'_\star$) obtained by our group using similar analysis to this article. See text for brief descriptions.

highly frequency-dependent dissipation, $Q'_\star \propto P_{\text{tide}}^{-3.1}$, for tidal periods $0.5 \text{ days} < P_{\text{tide}} < 2 \text{ days}$.

It should be noted that, while in Fig. 9 we plot the inferred tidal dissipation as a function of tidal frequency, that need not necessarily be the explanation of all differences observed. Each article analyzes a different collection of binary star or exoplanet systems with different selection biases involved. Given the wide variety of possible tidal dissipation physics (see Sec. 1), differences between measured dissipation in different studies may be caused by any systematic difference between the populations investigated, or even by trends within a population. For example, the dominant tidal period in each system is related to the orbital period, but eccentricity is also tightly correlated with orbital period. As a result, the binaries driving the tightly constrained Q'_\star at tidal periods $> 15 \text{ days}$ are the longest period binaries in our sample, which also have systematically higher eccentricities than the binaries dominating the constraints in PS22, and even more compared to the P18 systems which are virtually all circular. In turn, the orbital eccentricity determines the combination of tidal waves each component of the binary is subjected to.

7.2 Comparison with Studies By Other Groups

Our group is far from the only one attempting to infer how efficiently tidal perturbations are dissipated by studying signatures of tidal dissipation in observed populations of objects. An exhaustive review of all such efforts in the literature is beyond the scope of this article, but we highlight some of the most recent efforts here to allow comparison to our results.

One approach is to directly compare the predictions of a particular tidal dissipation model to observation. This was recently done by [Barker \(2022\)](#) who compared the predictions of inertial wave enhanced dissipation to observed tidal circularization, and found good agreement. In that model, the dissipation is strongly enhanced if the tidal period is more than half the spin period of the star. On the main sequence, that model predicts $Q'_\star \sim 10^7 (P_\star/10 \text{ days})^2$ for Sun-like stars, where P_\star is the spin period of the star. This corresponds to several times more efficient dissipation than what we find at the longest orbital periods in our sample, and several times less efficient than the dissipation PS22 find for main sequence binaries (assuming synchronous rotation).

[Meibom & Mathieu \(2005\)](#) and [Milliman et al. \(2014\)](#) used observed orbits of spectroscopic binary stars in open clusters to claim a detection of continued circularization during the main sequence for Sun-like stars that could be explained by $Q'_\star \sim \text{few} \times 10^5$ for tidal periods of several days. This overlaps reasonably well with the PP22 results and lies within a factor of two of the lower limit this study finds for such orbital periods.

[Zanazzi \(2022\)](#) recently combined the W19 eccentricities with similar constraints from TESS ([Justesen & Albrecht 2021](#)) to argue that the period-eccentricity distribution of binary stars should be split into two components: a cold core with very close to zero eccentricity out to orbital periods as large as 10 days, and an envelope of systems which is only circularized out to periods of 3 or 4 days, with a broad distribution of eccentricities after that. The cold core requires tidal dissipation similar to what PS22 and [Meibom & Mathieu \(2005\)](#) find, while the envelope needs much less efficient dissipation, perhaps arguing for a dissipation mechanism that only operates on some systems and not on others based on initial conditions.

[Hamer & Schlaufman \(2019\)](#) argue that the galactic velocity dispersion of Hot Jupiter host stars implies they are on average younger than field stars, interpreting this as evidence for tidal inspiral of Hot Jupiters over the main sequence lifetime of Sun-like stars. This in turn requires $Q'_\star < 10^7$, in agreement with all constraints mentioned above.

7.3 Caveats and Assumptions

The analysis presented here makes a number of assumptions. Below we discuss some of those assumptions.

The most central assumption we make is that each of the binaries in our input sample contains no other dynamically relevant objects and that tides are the only thing causing the orbit to evolve or stellar spin to deviate from that of an isolated star. While triple or higher multiplicity stellar systems are not uncommon, the W19 analysis used 4 years of ultra-high precision photometric measurements which result in high sensitivity to eclipse timing variations that would be produced by the presence of additional objects. Indeed, W19 encounter such objects and discard them from their sample. Nonetheless, some higher multiplicity systems likely still remain in the sample, though the configurations of those systems will be such that the extra objects likely do not affect the dynamics too strongly.

A critical component of our model affecting the predicted stellar spins is the loss of angular momentum to stellar winds. The model we use correctly captures the major features for stars spinning no slower than the Sun, but for slow rotators, ([van Saders et al. 2016](#); [Metcalfe & Egeland 2019](#)) argue spin-down stalls. Luckily, the slowest spinning star in our sample has a spin period of 21 days, which is shorter than the period at which spin-down may stall.

Different tidal dissipation theories predict effective Q'_\star that depends on a whole host of parameters (mass, age, metallicity, and spin of the star; amplitude of the tidal distortion; etc.). Here we allowed only for smooth dependence on the frequency with which each tidal wave propagates on the surface of the star, but all the other parameters change from one system to the next. Some parameters are even correlated with tidal frequency (e.g. tidal amplitude gets smaller at longer orbital periods which also correspond to longer tidal periods). Not accounting for such dependencies could skew, or even mask completely, the frequency dependence. The fact that the constraints we obtain for individual systems are consistent with each other is an encouraging sign that such dependencies are not dominant; however, that possibility cannot be ruled out entirely. Investigating dependen-

cies of Q'_\star on multiple parameters would require a significantly larger sample of systems than the 70 used here.

We assumed the tidal dissipation to be present only in the convective zone of the star. Although this is what equilibrium tide models predict for stars with convective envelopes, some dynamical tide models indicate that the dissipation will be dominated by interactions with g-mode waves inside the star's core. For the same exact Q'_\star , such models will predict significantly different surface spin for stars, because tides will deposit angular momentum in the core, which will be communicated to the envelope on some coupling timescale. Thus, somewhat more efficient dissipation will be required to explain the observed spins if tides couple to the core. Exploring the implications of tides coupling to the radiative core instead of the convective envelope is a separate project of comparable complexity to the one presented in this article. As such we consider it outside the scope at this moment and may pursue it in the future.

The treatment of angular momentum redistribution within stars in POET is quite simplistic. The core and the envelope are assumed to converge to synchronous rotation on a fixed timescale, and each zone is assumed to follow solid body rotation. While this is probably a reasonable assumption for the core, we know this picture is not correct for the convective envelope. For example, in the Sun, different parts of the convective zone spin differently, and are not even organized in spherical shells (see for example (Miesch 2005) for more details). Since we compare predicted to observed spins to infer the tidal dissipation efficiency, our results could be affected if important physics is not captured by the simplistic treatment used.

8 CONCLUSION

By combining catalogues from the literature of the physical properties and primary star spins of a collection of eclipsing binaries, we were able to infer how efficiently tidal perturbations dissipate energy. We find tight constraints for a frequency dependent modified tidal quality factor Q'_\star for tidal frequencies between 15 and 50 days, with $7.8 < \log_{10} Q'_\star < 8.1$ at the longest periods, with indications of decreasing by approximately 0.5 dex (dissipation efficiency enhanced by a factor of 3) for periods of 15 days. Below 15 days the precision with which the dissipation is measured is dramatically reduced: $5.7 < \log_{10} Q'_\star < 7.5$. The decreased precision is because most systems sensitive to such tidal periods are also in close enough orbits to have their spin synchronized with the orbit, reducing our ability to place a lower limit on Q'_\star (upper limit on the dissipation).

The constraints obtained in this article expand on previous constraints found by our group, which has embarked on a long-term effort to explore signatures of tidal dissipation in low mass stars in multiple settings, including tidal circularization in binary stars, the effects of tides on the spin exoplanet hosts and binary star systems, and others. Comparison between all constraints in this series to date is presented in Fig. 9. Interpreting the variations of Q'_\star from one system to the next as a frequency dependence, we find a consistent picture, with constraints from different contexts overlapping with each other for tidal frequencies probed by multiple analyses.

By combining multiple measurements of Q'_\star we plan to explore its dependencies on various parameters, helping to narrow down the dominant physical mechanisms for the dissipation in various regimes. Such a multi-faceted approach is made possible by the recent and ongoing explosion of observations (soon to be) produced by missions like *Kepler*, *TESS*, *Gaia*, *PLATO* etc.

In service of this long term goal, our analysis is designed to account for observational and model uncertainties as fully as possible,

taking special care to avoid conclusions not strongly supported by observations. We also avoid assuming any particular tidal dissipation model, relying on a general parametric prescription instead that is able to accommodate to a reasonable degree all the proposed models.

ACKNOWLEDGEMENTS

This research was supported by NASA grant 80NSSC18K1009.

The authors acknowledge the Texas Advanced Computing Center (TACC) at The University of Texas at Austin for providing HPC resources that have contributed to the research results reported within this paper. URL: <http://www.tacc.utexas.edu>

DATA AVAILABILITY

All tables of input parameters presented in this article are derivative of published tables already available in machine readable form through the VizieR online service. They are reproducible by applying simple filtering to those tables, and thus do not warrant creating and publishing independent copies.

We have created a zenodo archive (Patel et al. 2023) to accompany this article, which provides machine readable tables of the following:

- The generated MCMC samples for each binary in the original HDF5 format produced by the emcee package (Foreman-Mackey et al. 2013) (see <https://emcee.readthedocs.io/en/stable/user/backends/>).
- The 2.3%, 15.9%, 84.1%, and 97.7% quantiles of $\log_{10} Q'_\star$ for the given binary as a function of tidal period for each binary (i.e. the coordinates defining the quantile curves in Fig. 1 and 2).
- The burn-in period for each quantile vs. tidal period (i.e. the coordinates defining the burn-in curves in Fig. 3 and 4).
- The estimated standard deviation of the fraction of samples below each of the 4 target quantiles for each binary (i.e. the coordinates defining the curves in Fig. 5 and 6).
- The 2.3%, 15.9%, 84.1%, and 97.7% percentiles of the combined $\log_{10} Q'_\star$ constraint from all binaries vs tidal period (i.e. the coordinates of the quantile curves in Fig. 7).
- The combined constraint 2.3%, 15.9%, 84.1%, and 97.7% percentiles and the 2.3% and 97.7% percentiles of individual constraints at the tidal periods where the difference between the latter is smallest (i.e. the coordinates defining the curves and points in Fig. 8).

The version of POET used for calculating the orbital evolution is available through zenodo archive Penev et al. (2023).

REFERENCES

- Alexander M. E., 1973, *Astrophysics and Space Science*, 23, 459
 Alvarado-Montes J. A., 2022, *MNRAS*, 517, 2831
 Barker A. J., 2020, *Monthly Notices of the Royal Astronomical Society*, 498, 2270–2294
 Barker A. J., 2022, *ApJ*, 927, L36
 Barker A. J., Ogilvie G. I., 2011, *Monthly Notices of the Royal Astronomical Society*, 417, 745
 Beugé C., Nesvorný D., 2012, *ApJ*, 751, 119
 Benbakoura M., Réville V., Brun A. S., Le Poncin-Lafitte C., Mathis S., 2019, *A&A*, 621, A124
 Bolmont E., Gallet F., Mathis S., Charbonnel C., Amard L., Alibert Y., 2017, *A&A*, 604, A113
 Botev Z. I., Grotowski J. F., Kroese D. P., 2010, *The Annals of Statistics*, 38, 2916

- Davenport J. R. A., Hebb L., Hawley S. L., 2015, *The Astrophysical Journal*, **806**, 212
- Debes J. H., Jackson B., 2010, *ApJ*, **723**, 1703
- Duguid C. D., Barker A. J., Jones C. A., 2020, *Monthly Notices of the Royal Astronomical Society*, 497, 3400
- Eggleton P. P., Kiseleva L. G., Hut P., 1998, *Astrophysical Journal*, **499**, 853
- Essick R., Weinberg N. N., 2016, *Astrophysical Journal*, **816**, 18
- Fabrycky D., Tremaine S., 2007, *ApJ*, **669**, 1298
- Foreman-Mackey D., Hogg D. W., Lang D., Goodman J., 2013, *Publications of the Astronomical Society of the Pacific*, 125, 306
- Fuller J., 2017, *Monthly Notices of the Royal Astronomical Society*, 472, 1538
- Fuller J., Luan J., Quataert E., 2016, *MNRAS*, **458**, 3867
- Gallet F., Bouvier J., 2015, *Astronomy and Astrophysics*, **577**, A98
- Gallet, F. Bouvier, J. 2013, *A&A*, **556**, A36
- Goldreich P., Keeley D. A., 1977, *Astrophysical Journal*, **211**, 934
- Goldreich P., Soter S., 1966, *Icarus*, **5**, 375
- Goodman J., Dickson E. S., 1998, *Astrophysical Journal*, **507**, 938
- Hamer J. H., Schlaufman K. C., 2019, *AJ*, **158**, 190
- Hut P., 1981, *Astronomy and Astrophysics Journal*, **99**, 126
- Irwin J., Hodgkin S., Aigrain S., Hebb L., Bouvier J., Clarke C., Moraux E., Bramich D. M., 2007, *Monthly Notices of the RAS*, **377**, 741
- Justesen A. B., Albrecht S., 2021, *ApJ*, **912**, 123
- Kirk B., et al., 2016, *VizieR Online Data Catalog*, p. [J/AJ/151/68](https://vizier.cesr.cnrs.fr/vizieR/identifiers/J/AJ/151/68)
- Lai D., 2012, *Monthly Notices of the RAS*, **423**, 486
- Lecoanet D., Quataert E., 2013, *Monthly Notices of the Royal Astronomical Society*, **430**, 2363
- Lin D. N. C., Bodenheimer P., Richardson D. C., 1996, *Nature*, **380**, 606
- Lomb N. R., 1976, *Ap&SS*, **39**, 447
- Lurie J. C., et al., 2017, *The Astronomical Journal*, 154, 250
- Ma L., Fuller J., 2021, *ApJ*, **918**, 16
- Marcy G. W., Butler R. P., 1996, *ApJ*, **464**, L147
- Matijević G., et al., 2012, *Astrophysical Journal, Supplement*, **200**, 14
- Mayor M., Queloz D., 1995, *Nature*, **378**, 355
- McQuillan A., Aigrain S., Mazeh T., 2013, *MNRAS*, **432**, 1203
- Meibom S., Mathieu R. D., 2005, *ApJ*, **620**, 970
- Metcalfe T. S., Egeland R., 2019, *ApJ*, **871**, 39
- Miesch M. S., 2005, *Living Reviews in Solar Physics*, **2**, 1
- Milliman K. E., Mathieu R. D., Geller A. M., Gosnell N. M., Meibom S., Platais I., 2014, *AJ*, **148**, 38
- Ogilvie G. I., 2009, *Monthly Notices of the Royal Astronomical Society*, 396, 794–806
- Ogilvie G. I., 2012, *Monthly Notices of the Royal Astronomical Society*, 429, 613
- Ogilvie G. I., 2013, *Monthly Notices of the RAS*, **429**, 613
- Ogilvie G. I., Lesur G., 2012, *Monthly Notices of the Royal Astronomical Society*, **422**, 1975–1987
- Ogilvie G. I., Lin D. N. C., 2004, in Beaulieu J., Lecavelier Des Etangs A., Terquem C., eds, *Astronomical Society of the Pacific Conference Series Vol. 321, Extrasolar Planets: Today and Tomorrow*. p. 357
- Ogilvie G. I., Lin D. N. C., 2007, *The Astrophysical Journal*, **661**, 1180–1191
- Patel R., Penev K., 2022, *Monthly Notices of RAS*, **512**, 3651
- Patel R., Penev K., Schussler J., 2023, *Bayesian Samples and Data Behind Figures: Constraints on Tidal Quality Factor in Kepler Eclipsing Binaries using Tidal Synchronization: A Frequency-Dependent Approach*, doi:10.5281/zenodo.7742772, <https://doi.org/10.5281/zenodo.7742772>
- Paxton B., Bildsten L., Dotter A., Herwig F., Lesaffre P., Timmes F., 2011, *The Astrophysical Journal*, **192**, 3
- Penev K. M., Schussler J. A., 2022, *Monthly Notices of the RAS*, **516**, 6145
- Penev K., Sasselov D., Robinson F., Demarque P., 2009, *Astrophysical Journal*, **704**, 930
- Penev K., Zhang M., Jackson B., 2014, *Publications of the Astronomical Society of the Pacific*, **126**, 553–564
- Penev K., Bouma L. G., Winn J. N., Hartman J. D., 2018, *AJ*, **155**, 165
- Penev K., Vortebou Jackson B., Patel R., Bouma L., 2023, *kpenev/poet: Constraints on Tidal Quality Factor in Kepler Eclipsing Binaries using Tidal Synchronization: A Frequency-Dependent Approach*, doi:10.5281/zenodo.7742991, <https://doi.org/10.5281/zenodo.7742991>
- Prsa A., Matijević G., Latković O., Vilardell F., Wils P., 2011, *PHOEBE: PHysics Of Eclipsing BinariEs*, Astrophysics Source Code Library, record ascl:1106.002 (ascl:1106.002)
- Raftery A. E., Lewis S., 1991, Technical report, How many iterations in the Gibbs sampler?. WASHINGTON UNIV SEATTLE DEPT OF STATISTICS
- Rappaport S., et al., 2014, *The Astrophysical Journal*, **788**, 114
- Rasio F. A., Ford E. B., 1996, *Science*, **274**, 954
- Rieutord M., Valdetarro L., 2010, *Journal of Fluid Mechanics*, **643**, 363
- Schatzman E., 1962, *Annales d'Astrophysique*, **25**, 18
- Soderblom D. R., 2010, *Annual Review of Astronomy and Astrophysics*, **48**, 581
- Vick M., Lai D., Anderson K. R., 2019, *MNRAS*, **484**, 5645
- Vidal J., Barker A. J., 2020, *The Astrophysical Journal*, **888**, L31
- Windemuth D., Agol E., Ali A., Kiefer F., 2019, *Monthly Notices of the Royal Astronomical Society*, **489**, 1644–1666
- Witte M. G., Savonije G. J., 1999, *Astrophysical Journal*, **350**, 129
- Witte M. G., Savonije G. J., 2001, *Astrophysical Journal*, **366**, 840
- Zahn J. P., 1975, *A&A*, **41**, 329
- Zahn J.-P., 1989, *Astronomy and Astrophysics*, **220**, 112
- Zanazzi J. J., 2022, *ApJ*, **929**, L27
- van Saders J. L., Ceillier T., Metcalfe T. S., Silva Aguirre V., Pinsonneault M. H., García R. A., Mathur S., Davies G. R., 2016, *Nature*, **529**, 181

APPENDIX A: MODIFIED TIDAL DISSIPATION PRESCRIPTION

If $\alpha < 0$, Eq. 16 has a discontinuity at $\Omega_{m,m'} = 0$. This makes it possible for tides to hold the system in a spin orbit lock, keeping $\Omega_{m,m'} = 0$ for an extended period of time. POET handles this discontinuity by eliminating the stellar spin as a variable and checking at each time step that the lock is maintained. For $\alpha > 0$, there is no discontinuity. However, even in this case it often still happens that the system is held close to a lock for a long time, which forces the differential equation solver to use tiny time steps in order to maintain numerical accuracy. This in turn makes such cases very computationally expensive to simulate. In order to avoid this situation, we slightly modify Eq. 16 if $\alpha > 0$ to force a small, but finite dissipation as $\Omega_{m,m'} \rightarrow 0$:

$$\Delta_{m,m'} = \Delta_0 \begin{cases} \left(\frac{\Omega_{\min}}{\Omega_{\text{break}}}\right)^\alpha & \text{if } \Omega_{m,m'} < \Omega_{\min} \\ \left(\frac{\Omega_{m,m'}}{\Omega_{\text{break}}}\right)^\alpha & \text{if } \Omega_{\min} < \Omega_{m,m'} < \Omega_{\text{break}} \\ 1 & \text{if } \Omega_{m,m'} > \Omega_{\text{break}} \end{cases} \quad (\text{A1})$$

We pick $\Omega_{\min} = \frac{2\pi}{50d}$ in Eq. A1. This is small enough to not appreciably change the evolution, while at the same time eliminating most of the computational challenges.

This paper has been typeset from a $\text{\TeX}/\text{\LaTeX}$ file prepared by the author.